p-ISSN: 2963-7856| e-ISSN: 2961-9890
Available online at jerkin.org/index.php/jerkin
Jurnal Pengabdian Masyarakat dan Riset Pendidikan
Volume 5 No. 2, Oktober - Desember 2026, pp 5760-5769

Dynamic and Stability Analysis of a Non-Autonomous Nonlinear RLC Circuit with a Varactor Diode via the Atangana-Baleanu Fractional Derivative

Sri Puji Lestari[1*], Muhammad Dicky Nursyami[2]

[1,2] Department of Electrical Engineering, Universitas Islam Balitar, Jl. Imam Bonjol No. 16, Jl. Majapahit No. 2-4, Sananwetan, Kec. Sananwetan, Blitar City, East Java 66137, Indonesia.
E-mail: sripujilestari623@gmail.com
*Corresponding Author

https://doi.org/10.31004/jerkin.v5i2.8383

ARTICLE INFO

Article history:
Received: 14 Nov 2026
Revised: 20 Nov 2026
Accepted: 26 Nov 2026

Kata Kunci:
Rangkaian RLC Nonlinier, Dioda Varaktor, Osilator Helmholtz-Duffing, Turunan Fraksional Atangana-Baleanu, Diagram Bifurkasi, Eksponen Lyapunov, Penampang Poincaré.

Keywords:
Nonlinear RLC Circuit, Varactor Diode, Helmholtz-Duffing Oscillator, Atangana-Baleanu Fractional Derivative, Bifurcation Diagram, Lyapunov Exponent, Poincaré Section.

ABSTRACT

Studi ini meneliti dinamika dan stabilitas rangkaian RLC seri non-otonom yang mengandung dioda varaktor sebagai elemen kapasitif nonlinier, dengan efek memori non-lokal yang dimodelkan melalui turunan fraksional Atangana-Baleanu dalam pengertian Caputo (ABC). Hubungan muatan-tegangan dioda diturunkan dari kapasitansi sambungan yang bergantung pada tegangan, diintegrasikan, dan diinversi secara analitis hingga orde ketiga. Turunan ini menghasilkan suku nonlinier kuadrat dan kubik, di mana koefisien kubik menghilang untuk sambungan yang tiba-tiba dan menunjukkan perilaku pengerasan untuk profil doping yang lebih curam seperti sambungan hipertiba-tiba. Penerapan hukum tegangan Kirchhoff menghasilkan osilator Helmholtz-Duffing teredam dan terpaksa, di mana titik keseimbangan dan kriteria stabilitas lokal ditetapkan. Setelah normalisasi parameter, sistem fraksional diintegrasikan secara numerik menggunakan skema Adams-Bashforth-Moulton yang diadaptasi untuk operator ABC. Simulasi menunjukkan transisi dari osilasi periodik ke gerak kacau melalui kaskade penggandaan periode, yang dikonfirmasi oleh diagram bifurkasi, eksponen Lyapunov terbesar yang positif, dan struktur atraktor kacau pada penampang Poincaré, diikuti oleh krisis kembali ke orbit periode tunggal. Menurunkan orde fraksional menekan kekacauan menjadi osilasi periode tunggal dan secara bertahap mengurangi amplitudo respons, yang mengkonfirmasi peran stabilisasi memori fraksional.

This study examined the dynamics and stability of a non-autonomous series RLC circuit containing a varactor diode as a nonlinear capacitive element, with non-local memory effects modeled through the Atangana-Baleanu fractional derivative in the Caputo sense (ABC). The charge-voltage relationship of the diode was derived from its voltage-dependent junction capacitance, integrated, and analytically inverted up to the third order. This derivation produced quadratic and cubic nonlinear terms, in which the cubic coefficient vanished for an abrupt junction and exhibited hardening behavior for steeper doping profiles such as hyperabrupt junctions. Applying Kirchhoff's voltage law led to a damped, forced Helmholtz-Duffing oscillator, for which equilibrium points and local stability criteria were established. After parameter normalization, the fractional system was integrated numerically using an Adams-Bashforth-Moulton scheme adapted for the ABC operator. The simulations showed a transition from periodic oscillations to chaotic motion through a period-doubling cascade, confirmed by the bifurcation diagram, a positive largest Lyapunov exponent, and a chaotic attractor structure on the Poincaré section, followed by a crisis back to a single-period orbit. Lowering the fractional order suppressed chaos into single-period oscillations and gradually reduced the response amplitude, confirming the stabilizing role of fractional memory.

This is an open access article under the CC–BY-SA license.

How to Cite: Sri Puji Lestari, et al. (2026), Dynamic and Stability Analysis of a Non-Autonomous Nonlinear RLC Circuit with a Varactor Diode via the Atangana-Baleanu Fractional Derivative. 5(2). https://doi.org/10.31004/jerkin.v5i2.8383

INTRODUCTION

In electric circuit analysis, passive resistor-inductor-capacitor (RLC) circuits are usually modeled as linear systems described by integer-order differential equations. Under real physical conditions, component nonlinearity often causes the transient response and the oscillations to deviate strongly from a linear exponential decay (Danzi dkk., 2025). This behavior is widely encountered in high-frequency electronic devices, such as the voltage-controlled oscillator (*Voltage-Controlled Oscillator*/VCO) in integrated circuits (Duan dkk., 2024). The presence of nonlinear components such as semiconductor diodes or varactor diodes, whose capacitance depends on the applied voltage, can give rise to a rich variety of dynamics. At particular excitation amplitudes and frequencies, such circuits may exhibit nonlinear damped oscillations, hysteresis, bifurcations, and even a period-doubling cascade toward chaos (Hellen, 2024).

On the other hand, the dependence of the varactor diode capacitance on the reverse bias voltage is precisely what is exploited for tuning (*tunability*) in radio-frequency and microwave devices. In the *split-ring resonator* (SRR) based on a varactor, the variation of the capacitance over time produced by the bias voltage is used to generate frequency modulation, both on harmonic signals and on deterministic chaotic signals (Vovchuk dkk., 2020). This approach is favored because the design is compact, the frequency-deviation range is easy to adjust, and the fabrication cost is relatively low. In tunable microwave filters, semiconductor varactors likewise provide small dimensions, a wide tuning range, and a fast response obtained by adjusting the depletion-layer width of the p-n junction (Wang dkk., 2011). In addition, varactor diodes are used in metamaterial resonators for reconfigurable microwave circuits (Nesimoglu & Sabah, 2016) and in *metasurface* low-frequency radar absorbers whose resonance is modeled as a parallel RLC circuit (Lopez dkk., 2024).

Although circuit models based on integer-order differential equations have long been used, they cannot yet capture the memory effects and the non-local behavior of real materials and electronic components (Podlubny & Petráš, 2026). In practice, the voltage-current relationship of a component does not depend solely on the instantaneous state but is also governed by its previous history. A fractional-calculus approach is therefore needed so that energy dissipation and hereditary memory can be represented in better agreement with the physical behavior (Podlubny & Petráš, 2026).

In general, non-local fractional derivative operators are distinguished into singular-kernel operators, such as the power-law-based Caputo derivative, and non-singular-kernel operators (Hattaf, 2023; Shaikh dkk., 2025). The singular kernel of the classical operators often creates analytical as well as numerical difficulties at the initial point. To overcome this, (Atangana & Baleanu, 2016) introduced a fractional derivative operator in the Caputo sense (ABC) that employs a Mittag-Leffler function kernel, so that it is non-local and free of singularity. This ABC formulation can describe material heterogeneity and memory dynamics without a singularity at the start of the simulation, with a more flexible solution space than integer-order models (Asif dkk., 2025).

Research on the stability, bifurcation, and emergence of *chaos* in nonlinear fractional-order dynamical systems has grown considerably. Bifurcation diagrams, phase portraits, and the largest Lyapunov exponent are commonly used to detect stability transitions such as period-doubling and Neimark-Sacker bifurcations, and to distinguish the loss of stability of an equilibrium point from chaotic regimes (Gündüz dkk., 2026; Lestari dkk., 2025; Shi dkk., 2024). For the numerical simulations, schemes based on Lagrange polynomial interpolation for systems with the ABC operator have proven effective in capturing chaotic behavior (Boulaaras dkk., 2025). Besides Lyapunov exponents and bifurcation diagrams, the Poincaré section also plays an important role in mapping the dynamical structure of fractional systems, although its use in fractional-order systems is still relatively limited (Allogmany dkk., 2025).

Most studies of fractional-order RLC circuits still focus on linear capacitor elements or employ classical fractional operators. The interaction between the non-local memory effect of the ABC operator and the varactor diode nonlinearity in a non-autonomous RLC circuit has not yet been examined in an integrated manner. Therefore, this study formulates a model of a nonlinear non-autonomous series RLC circuit loaded with a varactor diode within the framework of the Atangana-Baleanu fractional derivative, and then examines its response and stability. Through bifurcation diagrams, Lyapunov exponent spectra, and Poincaré sections, this study observes the effect of varying the fractional order and the excitation amplitude on the stability threshold and on the emergence of *chaos*.

METHOD

Formulation of the Mathematical Model of the Varactor-Diode-Based Nonlinear RLC Circuit

Consider a closed series circuit consisting of a linear resistor R (Ω), a linear inductor L (H), and a varactor diode as the nonlinear capacitive energy-storage element. The circuit is supplied by an alternating voltage source $v_{\text{in}}(\tau) = V_m \sin(\omega\tau)$ with V_m the maximum voltage amplitude (V), $\omega = 2\pi f$ the excitation angular frequency (rad/s), and τ time (s). By Kirchhoff's voltage law, the algebraic sum of the potential differences around a single closed loop equals zero:

$$v_R(\tau) + v_L(\tau) + v_d(\tau) = v_{\text{in}}(\tau) \qquad (2.1)$$

The voltage across the resistor follows Ohm's law $v_R = R\, i(\tau)$, the voltage across the inductor follows Faraday's law of induction $v_L = L\, \mathrm{d}i(\tau)/\mathrm{d}\tau$, where $i(\tau)$ is the instantaneous current (A). The voltage of the varactor diode v_d depends nonlinearly on the charge $q(\tau)$ (C) accumulated in the depletion region of the *p-n* junction.

Physical characteristics and nonlinear modeling of the varactor diode

Unlike a parallel-plate capacitor, which has a constant capacitance, the width of the depletion region of a varactor diode changes with the voltage across it. The differential capacitance is defined as the rate of change of charge with respect to voltage, $C_v(v_d) = \mathrm{d}q/\mathrm{d}v_d$, and satisfies the empirical relation

$$C_v(v_d) = \frac{C_0}{\left(1 + \frac{v_d}{V_b}\right)^p} \qquad (2.2)$$

where C_0 is the junction capacitance at zero bias (F), V_b is the built-in contact potential (about $0{,}6 - 0{,}7$ V for silicon), and p is the doping-profile grading coefficient ($p = 0{,}5$ for an *abrupt* junction, $p = 1/3$ for a *linearly graded* junction, and $p \approx 2$ for a *hyperabrupt* varactor).

To obtain the voltage as a function of the charge, relation (2.2) is integrated from the condition $v_d = 0$ with $q(0) = 0$:

$$q(v_d) = \int_0^{v_d} \frac{C_0}{(1 + \xi/V_b)^p}\, \mathrm{d}\xi = \frac{C_0 V_b}{1-p}\left[\left(1 + \frac{v_d}{V_b}\right)^{1-p} - 1\right], \quad p \neq 1.$$

A binomial expansion up to the third order around $v_d = 0$ yields

$$q(v_d) = C_0 v_d - \frac{pC_0}{2V_b} v_d^2 + \frac{p(p+1)C_0}{6V_b^2} v_d^3 + \mathcal{O}(v_d^4) = a_1 v_d + a_2 v_d^2 + a_3 v_d^3 + \mathcal{O}(v_d^4),$$

with $a_1 = C_0$, $a_2 = -pC_0/(2V_b)$, and $a_3 = p(p+1)C_0/(6V_b^2)$.

The inverse series $v_d(q) = b_1 q + b_2 q^2 + b_3 q^3 + \mathcal{O}(q^4)$ is obtained by equating the coefficients of the powers of q, q^2, and q^3 in $q(v_d(q)) = q$:

$$b_1 = \frac{1}{a_1} = \frac{1}{C_0}, \qquad b_2 = -\frac{a_2}{a_1^3} = \frac{p}{2V_b C_0^2}, \qquad b_3 = \frac{2a_2^2 - a_1 a_3}{a_1^5} = \frac{p(2p-1)}{6V_b^2 C_0^3}.$$

With $\gamma_2 = b_2$ and $\gamma_3 = b_3$, the diode voltage in terms of the charge variable is written as

$$v_d(q) = \frac{1}{C_0} q + \gamma_2 q^2 + \gamma_3 q^3 \qquad (2.3)$$

The coefficient γ_2 describes the asymmetry of the capacitance-voltage curve of the p-n junction, whereas γ_3 describes the cubic nonlinearity that captures the hardening or softening of the electric field at large charge excursions. Based on the value of the doping gradient, three main cases arise. For $p = 1/2$ (an *abrupt* junction), the value of $\gamma_3 = 0$ is exactly zero so that only the quadratic nonlinearity remains. For $p < 1/2$, one has $\gamma_3 < 0$ (*softening*) and the potential of the system is unbounded from below, so the polynomial approximation is valid only for small excursions. Conversely, for $p > 1/2$, one has $\gamma_3 > 0$ (*hardening*) with a potential bounded from below, so the model can be used at large amplitudes. For the special case $\gamma_2 = \gamma_3 = 0$, Equation (2.3) reduces back to the classical linear capacitor law $v_c = q/C_0$.

Circuit equation and reduced form

Since $i(\tau) = \frac{\mathrm{d}q(\tau)}{\mathrm{d}\tau}$ and $\frac{\mathrm{d}i}{\mathrm{d}\tau} = \frac{\mathrm{d}^2 q}{\mathrm{d}\tau^2}$, substituting the voltage of each element into (2.1) gives

$$L\frac{\mathrm{d}^2 q}{\mathrm{d}\tau^2} + R\frac{\mathrm{d}q}{\mathrm{d}\tau} + \frac{1}{C_0} q + \gamma_2 q^2 + \gamma_3 q^3 = V_m \sin(\omega\tau) \qquad (2.4)$$

Copyright © 2026, Jurnal Pengabdian Masyarakat dan Riset Pendidikan
ISSN 2963-7856 (print), ISSN 2961-9890 (online)

Dividing both sides by L yields

$$\frac{\mathrm{d}^2q}{\mathrm{d}\tau^2} + 2\zeta\omega_0\frac{\mathrm{d}q}{\mathrm{d}\tau} + \omega_0^2 q + \beta_2 q^2 + \beta_3 q^3 = F_0\sin(\omega\tau) \qquad (2.5)$$

with the following reduced parameters: $\omega_0 = \frac{1}{\sqrt{LC_0}}$ is the natural resonance frequency (rad/s), $\zeta = (R/2)\sqrt{\frac{C_0}{L}}$ is the dimensionless damping ratio that determines the *underdamped*, *critically damped*, or *overdamped* regime at small excursions, $\beta_2 = \frac{\gamma_2}{L}$ and $\beta_3 = \frac{\gamma_3}{L}$ are the normalized quadratic and cubic nonlinearity coefficients, and $F_0 = \frac{V_m}{L}$ is the normalized excitation amplitude. Structurally, Equation (2.5) is a damped and forced Helmholtz-Duffing oscillator. Physically, L acts as the inertial mass, R as the viscous damping coefficient, and the varactor diode as an asymmetric nonlinear spring whose stiffness changes with the excursion.

State-space transformation and the Atangana-Baleanu operator

With $x_1(\tau) = q(\tau)$ and $x_2(\tau) = \mathrm{d}q(\tau)/\mathrm{d}\tau = i(\tau)$, Equation (2.5) becomes a two-dimensional first-order system

$$\frac{\mathrm{d}x_1}{\mathrm{d}\tau} = x_2, \qquad \frac{\mathrm{d}x_2}{\mathrm{d}\tau} = F_0\sin(\omega\tau) - 2\zeta\omega_0 x_2 - \omega_0^2 x_1 - \beta_2 x_1^2 - \beta_3 x_1^3 \qquad (2.6)$$

In semiconductor components and real inductors, the dielectric response of the p-n junction and the magnetic core losses give rise to relaxation and non-local memory effects. That is, the current and the charge at a given instant are influenced by the previous voltage history. The integer-order derivative in (2.6) is local at a single time instant and therefore cannot capture this memory effect. Hence, the $\mathrm{d}/\mathrm{d}\tau$ operator is replaced by the Atangana-Baleanu fractional derivative in the Caputo sense, ${}_0^{\mathrm{ABC}}D_\tau^\alpha$, for the fractional orders $\alpha_1, \alpha_2 \in (0,1]$. For any function $g \in H^1(0,T)$,

$${}_0^{\mathrm{ABC}}D_\tau^\alpha g(\tau) = \frac{B(\alpha)}{1-\alpha}\int_0^\tau \frac{\mathrm{d}g(\xi)}{\mathrm{d}\xi} E_\alpha\left[-\frac{\alpha}{1-\alpha}(\tau-\xi)^\alpha\right]\mathrm{d}\xi \qquad (2.7)$$

where $E_\alpha(z) = \sum_{k=0}^{\infty} z^k/\Gamma(\alpha k + 1)$ is the one-parameter Mittag-Leffler function and $B(\alpha) = 1 - \alpha + \alpha/\Gamma(\alpha)$ is the normalization function satisfying $B(0) = B(1) = 1$. Unlike the power-law kernel of the classical Caputo operator, the Mittag-Leffler kernel in (2.7) is non-singular at $\tau = \xi$. This property avoids the numerical spike at the initial point and can describe the memory transition from a stretched exponential to a power law smoothly. Applying definition (2.7) to (2.6) yields the fractional dynamic model

$$\begin{aligned} {}_0^{\mathrm{ABC}}D_\tau^{\alpha_1} x_1 = \Psi_1 = x_2, \qquad {}_0^{\mathrm{ABC}}D_\tau^{\alpha_2} x_2 = \Psi_2 \\ = F_0\sin(\omega\tau) - 2\zeta\omega_0 x_2 - \omega_0^2 x_1 - \beta_2 x_1^2 - \beta_3 x_1^3 \end{aligned} \qquad (2.8)$$

with the physical initial conditions $x_1(0) = q_0$ and $x_2(0) = i_0$ at $\tau = 0$. When $\alpha_1, \alpha_2 \to 1$, the ABC operator reduces to the ordinary derivative and Equation (2.8) returns exactly to the integer-order system (2.6).

Local Stability Analysis and Numerical Discretization Scheme of the Atangana-Baleanu Operator

Before the global-dynamics simulations (bifurcation diagrams, Lyapunov exponent spectra, Poincaré sections), an analysis of the equilibrium points and of the local stability conditions for the autonomous version of the system is required. A numerical discretization scheme is then constructed so that the non-autonomous fractional system in (2.8) can be integrated accurately and free of initial singularity.

Equilibrium points and Jacobian matrix

For the analytical determination of the static equilibrium points (x_1^*, x_2^*), the autonomous version ($F_0 = 0$) of (2.8) is considered:

$${}_0^{\mathrm{ABC}}D_\tau^{\alpha_1} x_1 = x_2, \qquad {}_0^{\mathrm{ABC}}D_\tau^{\alpha_2} x_2 = -\omega_0^2 x_1 - \beta_2 x_1^2 - \beta_3 x_1^3 \qquad (2.9)$$

By setting the right-hand side to zero we obtain $x_2^* = 0$ and

$$-\omega_0^2 x_1^* - \beta_2 (x_1^*)^2 - \beta_3 (x_1^*)^3 = 0 \qquad (2.10)$$

which factorizes as

$$x_1^*[\beta_3 (x_1^*)^2 + \beta_2 x_1^* + \omega_0^2] = 0 \qquad (2.11)$$

The system therefore possesses: (i) the trivial equilibrium point $E_0 = (0,0)$, which represents the zero-charge and zero-current condition of the varactor diode; and (ii) non-trivial equilibrium points, provided that $\beta_3 \neq 0$ and the discriminant $\Delta = \beta_2^2 - 4\beta_3\omega_0^2 \geq 0$, given by

$$x_{1,\pm}^{*} = \frac{-\beta_2 \pm \sqrt{\beta_2^2 - 4\beta_3\omega_0^2}}{2\beta_3}, \qquad x_2^{*} = 0 \qquad (2.12)$$

which yields up to two additional points $E_{\pm} = (x_{1,\pm}^{*}, 0)$ due to the asymmetry of the quadratic nonlinearity and of the cubic term characteristic of the varactor diode.

To test the local stability around $E^{*} = (x_1^{*}, 0)$, the Jacobian matrix of the autonomous vector field is formed:

$$J(E^{*}) = \begin{bmatrix} 0 & 1 \\ -\omega_0^2 - 2\beta_2 x_1^{*} - 3\beta_3 (x_1^{*})^2 & -2\zeta\omega_0 \end{bmatrix}_{(x_1^{*},0)} \qquad (2.13)$$

Defining the normalized effective differential stiffness

$$k_{\text{eff}}(x_1^{*}) = \omega_0^2 + 2\beta_2 x_1^{*} + 3\beta_3 (x_1^{*})^2 \qquad (2.14)$$

the characteristic equation and the eigenvalues of matrix (2.13) are

$$\lambda^2 + 2\zeta\omega_0\lambda + k_{\text{eff}}(x_1^{*}) = 0, \qquad \lambda_{1,2} = -\zeta\omega_0 \pm \sqrt{(\zeta\omega_0)^2 - k_{\text{eff}}(x_1^{*})} \qquad (2.15) - -(2.16)$$

Local stability criterion within the fractional calculus framework

For a fractional-order differential system with $\alpha \in (0,1]$, the local asymptotic stability around E^{*} is governed not only by the sign of the real part of the eigenvalues but also by their argument angle with respect to the negative real axis. The criterion commonly used is the Matignon-type condition

$$|\arg(\lambda_i)| > \frac{\alpha\pi}{2}, \qquad i = 1,2 \qquad (2.17)$$

Criterion (2.17) is essentially derived for Caputo-Riemann-Liouville type operators, yet it is commonly used as a working condition in the applied analysis of systems with the ABC operator. In the limit $\alpha \to 1$, this condition returns to the integer-order stability condition $\text{Re}(\lambda_i) < 0$.

From (2.16) and (2.17) the role of the physical parameters can be identified. At $E_0 = (0,0)$ one has $k_{\text{eff}}(0) = \omega_0^2 > 0$; as long as the damping $\zeta > 0$, the real parts of the eigenvalues are negative and the argument angles lie in quadrants II-III, so that (2.17) holds for every $\alpha \in (0,1]$. Lowering α actually widens the region of angular stability compared with the integer-order case, because the fractional memory effect weakens the tendency to instability of the linear oscillator near the origin. At $E_{\pm}$, the value of $k_{\text{eff}}(x_{1,\pm}^{*})$ depends directly on β_2, β_3, and on the position of the equilibrium point. If $k_{\text{eff}} < 0$, a positive real eigenvalue appears, which marks a *saddle*-type instability; nearby trajectories are pushed away from that point and, combined with the periodic excitation, may trigger large oscillations or chaotic behavior.

Numerical discretization scheme of the Atangana-Baleanu operator

When the external excitation is active ($F_0 \neq 0$), system (2.8) is non-autonomous and contains both quadratic and cubic terms, so that an exact analytical solution is difficult to obtain. The ABC fractional derivative equation is first converted into a Volterra integral form using the fundamental theorem of ABC fractional calculus. For ${}_0^{\text{ABC}}D_\tau^{\alpha} y(\tau) = \Psi(\tau, y(\tau))$ with $y(0) = y_0$,

$$y(\tau) - y(0) = \frac{1-\alpha}{B(\alpha)}\Psi(\tau, y(\tau)) + \frac{\alpha}{B(\alpha)\,\Gamma(\alpha)}\int_0^{\tau} (\tau - \xi)^{\alpha-1}\Psi(\xi, y(\xi))\,\mathrm{d}\xi \qquad (2.18)$$

At $\tau = 0$ the second term of the right-hand side vanishes and the first term gives a direct evaluation of the initial condition, so the scheme is free of singularity at the start of the simulation. On a uniform time grid $\tau_n = nh$, $n = 0,1,\ldots,N$, with $h = T/N$, evaluating (2.18) at τ_{n+1} and applying piecewise linear polynomial interpolation (the fractional trapezoidal/Adams-Bashforth-Moulton rule) to the memory integral yields the iterative formula

$$x_1(\tau_{n+1}) = x_1(0) + \frac{1-\alpha_1}{B(\alpha_1)}\Psi_1(\tau_n, x_1(\tau_n), x_2(\tau_n)) + \frac{\alpha_1 h^{\alpha_1}}{B(\alpha_1)\Gamma(\alpha_1+2)}\sum_{k=0}^{n}\left[\Psi_1(\tau_k)A_{n,k}^{(\alpha_1)} - \Psi_1(\tau_{k-1})B_{n,k}^{(\alpha_1)}\right] \qquad (2.19)$$

$$x_2(\tau_{n+1}) = x_2(0) + \frac{1-\alpha_2}{B(\alpha_2)}\Psi_2(\tau_n, x_1(\tau_n), x_2(\tau_n)) + \frac{\alpha_2 h^{\alpha_2}}{B(\alpha_2)\Gamma(\alpha_2+2)}\sum_{k=0}^{n}\left[\Psi_2(\tau_k)A_{n,k}^{(\alpha_2)} - \Psi_2(\tau_{k-1})B_{n,k}^{(\alpha_2)}\right] \qquad (2.20)$$

Copyright © 2026, Jurnal Pengabdian Masyarakat dan Riset Pendidikan
ISSN 2963-7856 (print), ISSN 2961-9890 (online)

with the memory quadrature weights for $\alpha \in (0,1]$

$$A_{n,k}^{(\alpha)} = (n+1-k)^{\alpha}(n-k+2+\alpha) - (n-k)^{\alpha}(n-k+2+2\alpha),$$
$$B_{n,k}^{(\alpha)} = (n+1-k)^{\alpha+1} - (n-k)^{\alpha}(n-k+1+\alpha), \qquad (2.21)$$

with the lower-limit convention $\Psi_m(\tau_{-1},\cdot) = \Psi_m(\tau_0,\cdot)$ for $m = 1,2$. The first term in (2.19)-(2.20) is evaluated at the already known step n, so the scheme is explicit. The cumulative summation $k = 0, \dots, n$ preserves the entire memory history of the system, while the excitation term $\sin(\omega\tau_k)$ is evaluated directly at each time step.

The scheme is validated by comparing the case $\alpha_1 = \alpha_2 = 1$ against the fourth-order Runge-Kutta method. For moderate excitation with step $h = 0{,}02$, the maximum error was recorded at about $3{,}4 \times 10^{-3}$. Because the scheme becomes unstable for $\alpha \lesssim 0{,}7$ at the step size used, the numerical simulations were restricted to the range $\alpha \geq 0{,}8$.

Parameter normalization for the simulation

So that the coefficients lie on a unit scale, time and charge are rescaled to $\tau' = \omega_0\tau$ and $x = q/(C_0V_b)$. By substituting γ_2 and γ_3 from the previous derivation of the varactor diode characteristics, together with the relation $LC_0\omega_0^2 = 1$, Equation (2.5) can be written as

$$x'' + 2\zeta x' + x + B_2x^2 + B_3x^3 = F\sin(\Omega\tau') \qquad (2.22)$$

with the dimensionless coefficients

$$B_2 = \frac{p}{2}, \qquad B_3 = \frac{p(2p-1)}{6}, \qquad F = \frac{V_m}{V_b}, \qquad \Omega = \frac{\omega}{\omega_0}$$

Equation (2.22) shows that the level of nonlinearity of the system is governed by the doping profile p. For a *hyperabrupt* varactor with $p = 2$, one obtains $B_2 = B_3 = 1$ with a potential bounded from below, so the simulation can be run without any local amplitude restriction. All simulations in the Results and Discussion section use form (2.22), with the symbols F_0, ω, and τ in the preceding description corresponding, respectively, to F, Ω, and τ'.

RESULTS AND DISCUSSION

Scheme (2.19)-(2.21) is applied to the normalized system (2.22) with the physical parameters given in Table 1. The choice $L = 1$ mH and $C_0 = 1$ nF gives $\omega_0 = 10^6$ rad/s ($f_0 \approx 159$ kHz); $R = 200\,\Omega$ gives $\zeta = 0{,}1$; $V_b = 0{,}7$ V (silicon); and a *hyperabrupt* profile $p = 2$ gives $B_2 = B_3 = 1$. The excitation frequency is set to $\Omega = 0{,}8$ and the amplitude F is varied as the control parameter. The scheme is integrated with a step of $h \approx 0{,}025$ of the excitation period; 150-200 transient periods are discarded before the steady-state statistics are taken.

Table 1. Simulation parameter values.

Quantity	Symbol	Value	Remarks
Inductance	L	1 mH	linear inductor
Zero-bias capacitance	C_0	1 nF	varactor
Resistance	R	$200\,\Omega$	gives $\zeta = 0{,}1$
Contact potential	V_b	0,7 V	silicon
Doping profile	p	2	*hyperabrupt*, $B_2 = B_3 = 1$
Natural frequency	ω_0	10^6 rad/s	$f_0 \approx 159$ kHz
Excitation frequency	Ω	0,8	normalized
Excitation amplitude	F	$1 - 8$	control parameter

Time Series and Phase Portraits

Figure 1 shows the time series of $x_1(\tau)$ over the last 12 periods together with the phase portraits (x_1, x_2) for four values of F. For $F = 2$, the trajectory forms a single closed curve, indicating period-1 (P1) motion. For $F = 4{,}5$, the phase portrait splits into two folds (P2), and then into four folds (P4) at $F = 6$. When $F = 6{,}4$, the trajectory fills a region of the phase space without repeating itself and forms a chaotic attractor that is sensitive to the initial conditions because of the interaction between the quadratic and cubic terms. The value of the fractional order $\alpha < 1$ reflects the strength of the non-local memory effect; the smaller α, the greater the influence of the history and the more the peak amplitude and the attractor density change, as discussed in the Effect of the Fractional Order subsection.

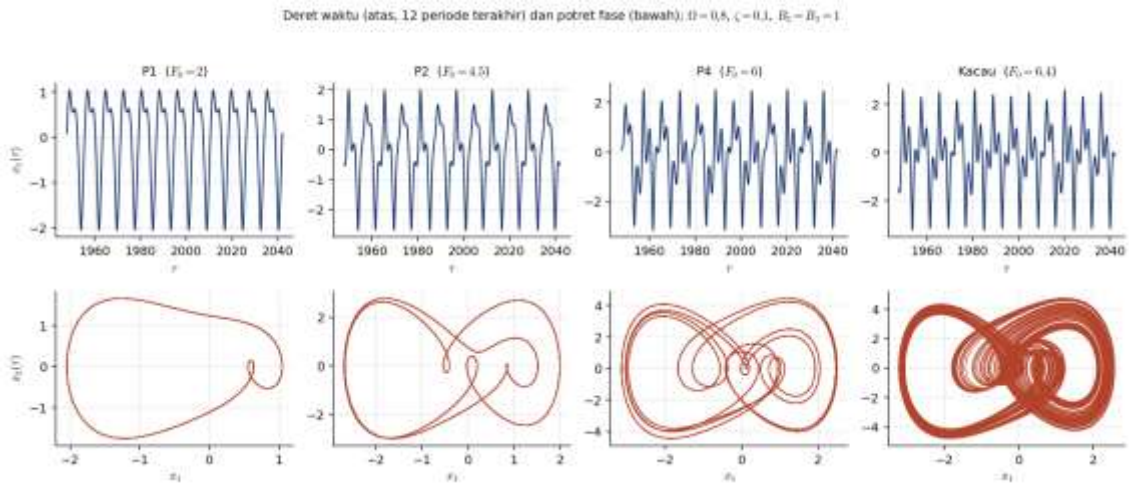


Figure 1. Time series and phase portraits for the four dynamical regimes.

Bifurcation Diagram

Figure 2 presents a snapshot of x_1 on the Poincaré section over the range $F \in [1,8]$ as the excitation amplitude is varied in steps. The period-doubling cascade P1 → P2 → P4 → ⋯ is observed, ending in a chaotic window around $F \approx 6{,}05 - 6{,}65$ (yellow shading), where the points spread out into a continuous band. Entering $F \gtrsim 6{,}7$, an attractor crisis occurs that makes the trajectory jump back onto the large-amplitude period-1 branch. This pattern indicates that the transition to *chaos* proceeds through period doubling rather than through a Hopf bifurcation at an equilibrium point. The result agrees with the previous local stability analysis: for $p = 2$ one has $B_2^2 - 4B_3 = -3 < 0$, so that only the point E_0 appears and remains stable ($k_{\text{eff}} = 1 > 0$ in normalized units). Narrow periodic windows and indications of attractor coexistence are also visible near the edges of the chaotic window.

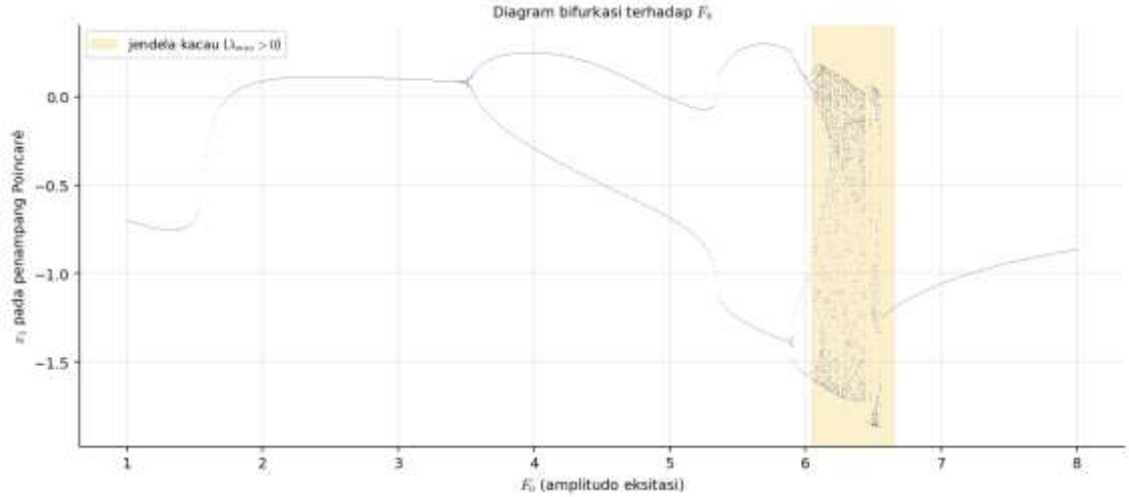


Figure 2. Bifurcation diagram against the excitation amplitude F.

Lyapunov Exponent Spectrum

As a quantitative confirmation, the largest Lyapunov exponent ($\lambda_{\max}$) is computed using the method of two nearby trajectories with renormalization at every excitation period (Benettin's method), which for a periodically forced system is equivalent to the exponent of the stroboscopic map. The result is shown in Figure 3. In the stable periodic regime, the value $\lambda_{\max} \approx -0{,}1$ describes the transverse contraction toward the orbit. Over some intervals such as $2{,}7 \lesssim F \lesssim 4{,}3$, the value approaches zero, which indicates weak contraction or quasi-periodic motion rather than *chaos*. The chaotic window is identified by $\lambda_{\max} > 0$ at $F \approx 6{,}1 - 6{,}6$ with a peak of $\lambda_{\max} \approx 0{,}0587$ at $F = 6{,}4$. After passing the crisis at $F \gtrsim 6{,}7$, the exponent returns to negative values. This spectral pattern is consistent with the bifurcation diagram in Figure 2.

Copyright © 2026, Jurnal Pengabdian Masyarakat dan Riset Pendidikan
ISSN 2963-7856 (print), ISSN 2961-9890 (online)

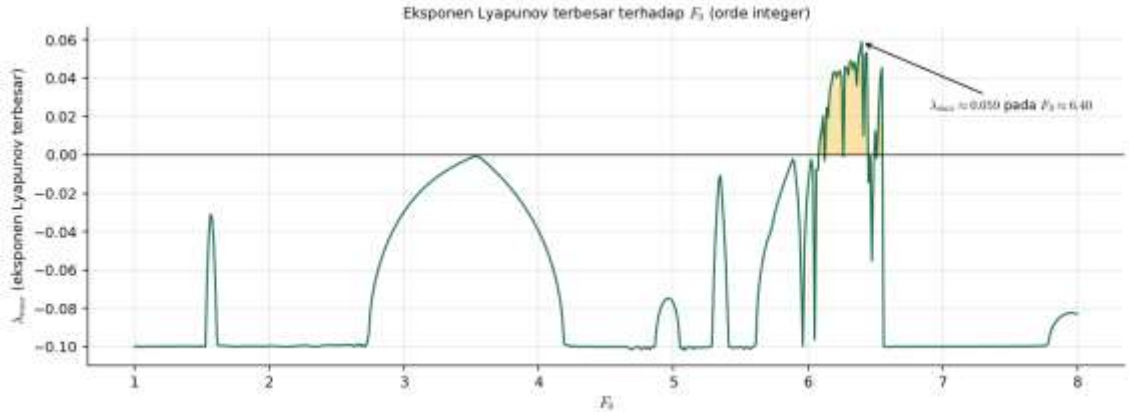


Figure 3. Largest Lyapunov exponent against F for the integer order.

Poincaré Section

Figure 4 shows the Poincaré section obtained by sampling (x_1, x_2) stroboscopically at every multiple of the excitation period $T = 2\pi/\Omega$. The P1 regime yields one point, P2 two points, and P4 four points, in agreement with the time series and the bifurcation diagram. At $F = 6{,}4$, the distribution of points forms a folded pattern with fractal geometry, which is the signature of a chaotic attractor. This section reinforces the visual reading of the bifurcation diagram and of the Lyapunov spectrum while also complementing a diagnostic analysis that is still rarely applied to fractional systems (Allogmany et al., 2025).

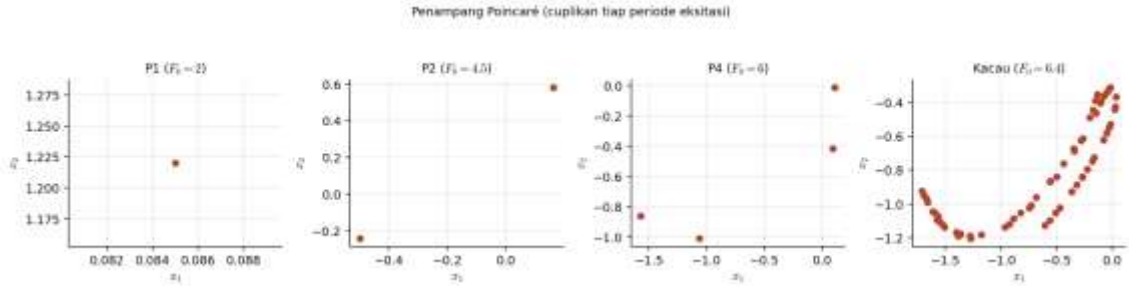


Figure 4. Poincaré sections for the four dynamical regimes.

Effect of the Fractional Order

Figure 5 compares the phase portraits and the time series for $\alpha_1 = \alpha_2 = \alpha$ at $F = 6{,}4$. For $\alpha = 1$ the system is in the chaotic regime. When α is reduced to 0,9 and 0,8, the chaotic attractor disappears and the system settles onto a period-1 orbit with a smaller amplitude. The number of Poincaré points and the swing width of x_1 are summarized in Table 2.

Table 2. Effect of the fractional order at $F = 6{,}4$; for $\alpha = 0{,}7$ the scheme becomes unstable at the time step used.

α	**Number of Poincaré points**	**Regime**	**Amplitude of Δx_1**
1,00	47	chaotic	5,833
0,95	1	period-1	4,435
0,90	1	period-1	3,972
0,80	1	period-1	3,614

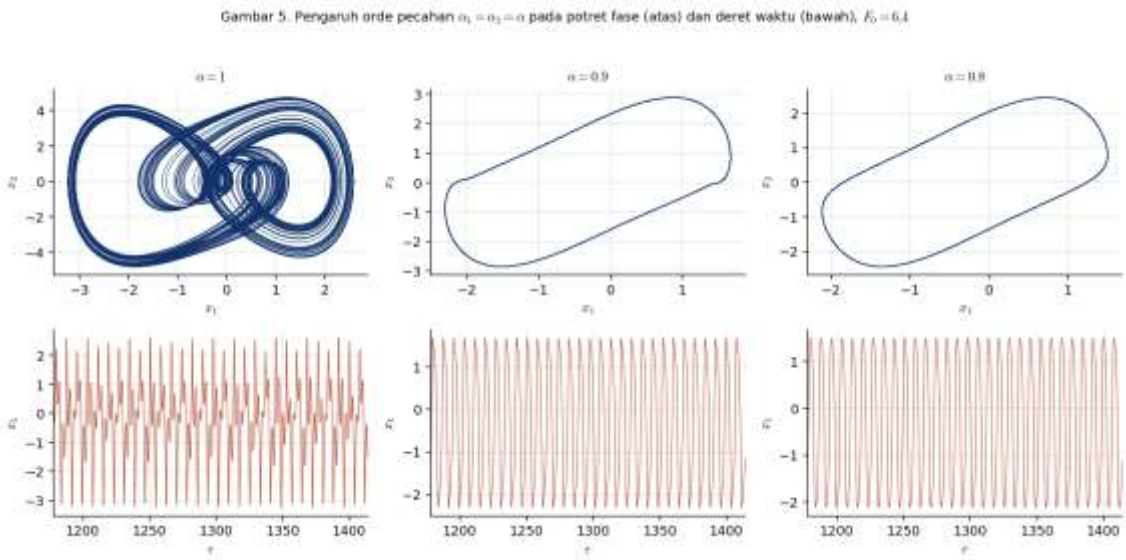


Figure 5. Effect of fractional memory on the attractor and on the response amplitude.

Physically, reducing α strengthens the influence of the history on the response of the diode junction and of the inductor. This memory effect acts like an additional damping that holds back the growth of the oscillations and stabilizes the orbit that was previously chaotic at $\alpha = 1$. This finding is consistent with the role of α in criterion (2.17), where the stability region widens as α is decreased. The result remains a numerical prediction of the ABC-ABM scheme, so experimental testing on a real varactor circuit is still required at the next stage.

CONCLUSION

A model of a non-autonomous series RLC circuit with a varactor diode has been formulated within the framework of the Atangana-Baleanu fractional derivative. The analytical derivation of the charge-voltage relation yields the cubic coefficient $\gamma_3 = \frac{p(2p-1)}{6V_b^2 C_0^3}$, which vanishes for an *abrupt* junction and is positive for a *hyperabrupt* profile, so that the nonlinear character of the system depends directly on the diode doping profile. The stability analysis shows that the point E_0 remains stable as long as $\zeta > 0$ for all $\alpha \in (0,1]$, whereas non-trivial equilibrium points appear only if $\beta_2^2 \geq 4\beta_3\omega_0^2$. Numerical simulations with realistic physical parameters show a period-doubling cascade leading to the chaotic window at $F \approx 6{,}05 - 6{,}65$, with a maximum Lyapunov exponent $0{,}0587$ and a chaotic attractor structure on the Poincaré section. Reducing the fractional order to $\alpha = 0{,}9$ and $0{,}8$ suppresses the chaotic behavior into period-1 oscillations and reduces the response amplitude, which confirms the stabilizing role of the fractional memory effect. For further research, the ABC-ABM scheme can be compared with the Grünwald-Letnikov scheme, extended by a full Lyapunov spectrum computation for the fractional system, and complemented by parameter identification on a physical circuit prototype.

ACKNOWLEDGMENTS

The authors would like to thank Universitas Islam Balitar for supporting this research through the funding granted under the Rector's Decree No. 074/SK/UNISBA/IV/2026 dated 8 April 2026, and the Department of Electrical Engineering, Faculty of Engineering and Informatics, for the facilities provided during the research and the preparation of this article.

REFERENCES

Allogmany, R., Sarrah, A., Abdoon, M. A., Alanazi, F. J., Berir, M., & Alharbi, S. A. (2025). A Comprehensive Analysis of Complex Dynamics in the Fractional-Order Rössler System. *Mathematics*, *13*(19), 1–25. https://doi.org/10.3390/math13193089

Asif, M., Popa, I. L., Ismail, E. A. A., Awwad, F. A., & Ishtiaq, U. (2025). Insights from Atangana-

Copyright © 2026, Jurnal Pengabdian Masyarakat dan Riset Pendidikan
ISSN 2963-7856 (print), ISSN 2961-9890 (online)

Baleanu fractional derivatives modeling of influenza epidemics and sensitivity analysis. *Scientific Reports*, *15*(1). https://doi.org/10.1038/s41598-025-18512-x

Atangana, A., & Baleanu, D. (2016). New fractional derivatives with non-local and non-singular kernel: Theory and application to heat transfer model. *Thermal Science*, *20*(2), 763–769. https://doi.org/10.2298/TSCI160111018A

Boulaaras, S., Sriramulu, S., Arunachalam, S., Allahem, A., Alharbi, A., & Radwan, T. (2025). Chaos and stability analysis of the nonlinear fractional-order autonomous system. *Alexandria Engineering Journal*, *118*(December 2024), 278–291. https://doi.org/10.1016/j.aej.2025.01.060

Danzi, F., Tao, H., Silva, C. E., & Gibert, J. M. (2025). Kirigami oscillators: nonlinear free and forced responses. *Nonlinear Dynamics*, *113*(16), 20711–20727. https://doi.org/10.1007/s11071-025-11221-0

Duan, Z., Li, H., He, S., Long, Y., Yu, X., & Ke, Q. (2024). Integrated Circuit of a Chua's System Based on the Integral-Differential Nonlinear Resistance with Multi-Path Voltage-Controlled Oscillator. *Micromachines*, *15*(3). https://doi.org/10.3390/mi15030401

Gündüz, H., Kaya, G., & Çelik, E. (2026). *Article in Press Bifurcation and chaos control in a conformable fractional-order logistic system*. 0–21.

Hattaf, K. (2023). A New Class of Generalized Fractal and Fractal-Fractional Derivatives with Non-Singular Kernels. *Fractal and Fractional*, *7*(5), 1–16. https://doi.org/10.3390/fractalfract7050395

Hellen, E. H. (2024). RLC resonator with diode nonlinearity: Bifurcation comparison of numerical predictions and circuit measurements. *Chaos*, *34*(7). https://doi.org/10.1063/5.0206829

Lestari, S. P., Suryanto, A., & Darti, I. (2025). Stability and Bifurcation Analysis of a Discrete Fractional Order Predator-Prey Leslie-Gower Model With Fear Effect, Allee Effect, and Interspecies Rivalry. *Communications in Mathematical Biology and Neuroscience*, *2025*, 1–21. https://doi.org/10.28919/cmbn/9147

Lopez, T., Lepetit, T., Ratni, B., & Burokur, S. N. (2024). Design and measurement of a tunable metasurface low-frequency radar absorber. *Journal of Applied Physics*, *135*(12). https://doi.org/10.1063/5.0196932

Nesimoglu, T., & Sabah, C. (2016). A tunable metamaterial resonator using varactor diodes to facilitate the design of reconfigurable microwave circuits. *IEEE Transactions on Circuits and Systems II: Express Briefs*, *63*(1), 89–93. https://doi.org/10.1109/TCSII.2015.2503058

Podlubny, I., & Petráš, I. (2026). Fractional-Order Memory Elements and Electrical Circuits for Future Electronics and Industrial Automation: A Survey. *Fractal and Fractional*, *10*(11), 734. https://doi.org/10.3390/fractalfract10110734

Shaikh, A., Waghule, S., Patil, D., & Nisar, K. S. (2025). A Study of the Atangana Baleanu Fractional Differential Equation with an Application in Gas Dynamic Problem. *Baghdad Science Journal*, *22*(7), 2386–2401. https://doi.org/10.21123/2411-7986.5004

Shi, Y., Liu, X., & Wang, Z. (2024). Bifurcation Analysis and Chaos Control of a Discrete Fractional-Order Modified Leslie–Gower Model with Nonlinear Harvesting Effects. *Fractal and Fractional*, *8*(12). https://doi.org/10.3390/fractalfract8120744

Vovchuk, D., Haliuk, S., Robulets, P., & Politanskyi, L. (2020). Frequency Modulation Approach Based on Split-Ring Resonator Loaded By Varactor Diode. *Informatyka, Automatyka, Pomiary w Gospodarce i Ochronie Srodowiska*, *10*(3), 74–77. https://doi.org/10.35784/iapgos.2003

Wang, X., Bao, P., Jackson, T. J., & Lancaster, M. J. (2011). Tunable microwave filters based on discrete ferroelectric semiconductor varactors. *IET Microwaves, Antennas and Propagation*, *5*(7), 776–782. https://doi.org/10.1049/iet-map.2010.0417